

Investigation of Hot Pressed Membrane Electrode Assemblies using X-ray Computed Tomography

Q. Meyer¹, N. Mansor¹, F. Iacoviello¹, P.L. Cullen¹, R. Jarvis¹, D. Finegan¹, C. Tan¹,
J. Bailey¹, P. R. Shearing^{*1}, D. J. L. Brett^{*1}

¹Electrochemical Innovation Lab, Department of Chemical Engineering, UCL,
London, WC1E 7JE, United Kingdom.

* Author to whom correspondence should be addressed

Tel.: +44(0)20 7679 3310

Web: www.ucl.ac.uk/electrochemical-innovation-lab

Email: d.brett@ucl.ac.uk; p.shearing@ucl.ac.uk

Abstract

The hot pressing process for fabricating membrane electrode assemblies (MEAs) has been widely adopted, yet little is known of its effects on the microstructural properties of the different components of the MEA. In particular, the interaction of the electrolyte, electrode and gas diffusion layer (GDL) due to lamination is difficult to probe as conventional imaging techniques cannot access the internal structure of the MEA.

Here, a novel approach is used, which combines characterisation of hot-pressed membrane electrode assemblies using X-ray computed tomography, thermogravimetric analysis, differential scanning calorimetry and atomic force microscopy, with electrochemical performance measurements from polarisation

curves and high-frequency impedance spectroscopy. Membrane electrode assemblies hot pressed at 100 °C, 130 °C and 170 °C reveal significant differences in microstructure, which has a consequence for the performance. When hot pressed at 100°C, which is lower than the glass transition temperature of Nafion (123 °C), the catalyst only partially bonds with the Nafion membrane, leading to increased Ohmic resistance. At 170 °C, the Nafion membrane intrudes into the electrode, forming pinholes, degrading the catalyst layer and filling pores in the GDL. Finally, at 130 °C, the interfacial contact is optimum, with similar roughness factor between the catalyst and Nafion membrane surface, indicating effective lamination of layers.

Keywords

Membrane electrode assembly; hot-pressing; X-ray computed tomography; roughness factor; Nafion.

1.1. Introduction

Polymer electrolyte fuel cells (PEFC) fuelled with hydrogen are among the most promising energy conversion technologies for a broad range of applications, including portable, stationary and automotive power delivery.

In order to maximise performance and durability, it is crucial to have an optimised process for the manufacture of membrane electrode assemblies (MEAs). The hot pressing process [1] bonds together the gas diffusion medium (gas diffusion layer (GDL) / micro-porous layer), the catalyst layer and the electrolyte membrane (usually Nafion) to form the MEA. Compression pressure, time and temperature are the key parameters that determine the product of hot pressing: of these, the temperature is most commonly used to optimise the process [2], typically by a trial and error approach. In spite of the ubiquity of the hot pressing process, little is understood regarding its influence on the resulting MEA structure. With an increasing array of materials available to fabricate MEAs, there is a need for more robust methods of

analysis to relate hot pressing conditions to the structure of the MEA and the consequent electrochemical performance and durability.

Here, high resolution 3-dimensional imaging of MEAs has been achieved using X-ray computed tomography (X-ray CT). Hot pressing temperatures of 100 °C, 130 °C and 170 °C (at 2757 kPa for 3 minutes) were studied, representing the range typically employed in practice for Nafion-based MEAs [1,3–16]. The approach allows for the segmentation of the electrolyte membrane, micro-porous layer / catalyst (MPLC) and gas diffusion layer, so as to study the interpenetration of each phase and the beneficial/detrimental structural properties that relate to electrochemical performance.

1.2. Membrane electrode assembly

The MEA is composed of a symmetrical structure with the electrolyte membrane in the centre, and the catalyst medium, gas diffusion layer and micro-porous layers on both sides of the membrane (Figure 1).

The electrically conducting, porous gas diffusion layer [17] provides reactant transport and acts as an effective current collector, whilst also improving water management by controlling the water flow [18]. The structure of the GDL, fibre geometry and porosity [19], as well as the effects of applied compression [20] have been widely investigated to understand how to optimise gas, water and electron transport. Engineering of GDL materials has been of particular focus, as its structure and PTFE content directly affect water management and fuel cell performance [21–24]. The GDL is usually composed of carbon fibres around 5-10 μm in diameter, coated with a PTFE/carbon-based ‘micro-porous’ layer [25].

The catalyst layer, in direct contact with the membrane and the GDL, is typically composed of a thin film (5-20 μm) [26,27] of highly dispersed platinum nano-particles (~3-5 nm) deposited on carbon particles (~30-50 nm) [28,29], with a Nafion ionomer additive to enhance the triple phase boundaries between the electrolyte, catalyst and the gaseous fuel [30,31]. It is either coated onto the microporous medium of the GDL or onto the Nafion membrane, via hand-painting, air-brushing, screen printing or sputtering [6,11,32–34]. The fabrication method used imparts different advantages; for example, coating the catalyst layer directly onto the Nafion membrane can improve the ionic contact at this interface, potentially creating a larger electrochemical surface area and lower contact resistance [6]. In contrast, coating the catalyst layer onto the carbon fibres of the GDL may make handling large amounts of materials easier, and reduce manufacturing cost. Furthermore, coating large amounts of gas diffusion material is easier than coating Nafion, due to the dimensional instability of the membrane. In addition, GDEs are easier to store than Nafion. Coating the catalyst onto a porous media may lead to material loss, penetrating too far from the electrode surface into the carbon fibre network. On the other hand, a controlled penetration depth may create a better electrode with lower charge transfer resistance, instead of a surface electrode in the case of the catalyst coated onto the membrane.

The hot pressing process will directly affect the quality of the MEA and impact on the electrode structure, catalyst utilization, migration and coalescence, consequently influencing the transport of ions, electrons, water and reactants in the system [16].

A wide range of process conditions are reported in the literature with hot press compression pressure ranging from 1380 kPa to 49,000 kPa, temperature from 90 °C to 170 °C, and time of compression from 90 s to 360 s [1–16,35–41]. Depending

on the materials used, a large number of internal parameters affect the hot-pressing process, which explains why such a wide range of conditions are reported.

1.3. Internal parameters affecting hot-pressing.

Figure 1 illustrates the different components of the MEA. Considering the catalyst layer as an example, the following parameters have an impact on the quality of the MEA obtained after hot pressing: layer initial thickness, crack size and distribution [30,42,43], extent of intrusion into the carbon fibres and micro-porous layer [44], the catalyst deposition method [32, [45], micro-porous layer porosity [46]. Collectively, these will affect the bonding process and different hot pressing conditions will be required to optimise the system.

Hot pressing temperature has a critical effect on the electrolyte membrane as it undergoes macro-structural changes before and after its glass transition (typ. Nafion ionomer 117-127 °C) [8,36,47,48] which affects its ability to flow and bond. The ionomer content within the catalyst layer will also affect the quality of the bonding process between the catalyst and the electrolyte membrane, as the Nafion ionomer with the catalyst will bond with the Nafion membrane [39,49–51].

Attempts to optimise the hot-pressing process include design-of-experiments [4,36] correlated with structural (e.g. SEM) and electrochemical analysis (electrochemical surface area and impedance spectroscopy) [52]. These studies have shown that the pressing temperature has the most important influence on the bonding process between electrode and electrolyte [2,36,52].

1.4. High resolution imaging of the membrane electrode assembly

Until recently, the main technique used to determine the structure of components within an MEA was scanning electron microscopy (SEM), frequently coupled with energy dispersive X-ray spectroscopy (EDS) analysis. SEM is useful in obtaining surface structural data, layer thickness, 'smoothness' of different interfaces, the orientation of carbon fibres and the PTFE content [18,19,44,46,53–60], catalyst surface [43], MEA structure [4,6,36] and degradation [54], but fails to reveal the porosity, connectivity and most importantly, the cross-sectional or surface view does not allow the internal structure to be quantified. Focused Ion Beam (FIB) SEM has also been used to study the structure of the micro-porous layer and catalyser layer [46,61–63], revealing nano-porosity, effective diffusivity, permeability and capillary radius, yet this method is destructive.

Micro- and nano-X-ray CT are non-destructive methods that can achieve sufficiently high resolution for imaging carbon fibres, which typically have diameters between 5 and 10 μm and have been increasingly used to characterise GDLs [20,46,64–67]. Recent work from the authors has linked GDL structure and PTFE content to water distribution using neutron imaging and X-ray CT [44]. Furthermore, X-ray CT has also been used to characterise different catalyst deposition methods [32], degradation mechanisms, crack length and catalyst distribution [30].

2. Experimental

2.1. Material

Dry Nafion NRE-212 membrane (Dupont, USA), was used as the electrolyte without pre-treatment. The MEAs were produced in-house using the electrolyte and ELE0162 Johnson Matthey gas diffusion electrodes (gas diffusion layer coated with catalyst layer $0.4 \text{ mg}_{\text{Pt}} \text{ cm}^{-2}$), with an active area of 5.29 cm^2 . The three MEAs were

hot-pressed (Carver 4122CE, USA) for 3 min with an applied pressure of 2757 kPa. at 100 °C, 130 °C and 170 °C, respectively. Two MEAs at each temperature were fabricated, one for use in fuel cell testing and one for the X-ray CT scans.

2.2. Characterisation methods.

Testing of cell performance.

Fuel cell measurements were carried out using a Scribner Associates 890e test station (Scribner, USA). The cell temperature was set at 80°C, and the anode and cathode were fed with humidified (98% relative humidity) H₂ and air, both at 2.0 stoichiometry. The minimum flow rate for both gases is 0.05 L min⁻¹. Prior to measurements, the MEA was activated by maintaining the cell current density in the sequence of 50 mA cm⁻², 100 mA cm⁻², 300 mA cm⁻², 500 mA cm⁻², and 700 mA cm⁻² for 30 minutes each, or until the voltage reaches a plateau. The polarisation curves were then taken by scanning the current density from 0 to 1 A cm⁻², with a step size of 18 mA cm⁻², with a current hold of 30 seconds at each point. The polarisation was halted when the voltage dropped below 0.2 V. Each polarisation was repeated twice, and the average polarisation was calculated. The high frequency resistance was measured every second.

Scanning electron microscopy (SEM)

For SEM imaging, the GDL was cut into circular samples of 2 mm diameter and attached onto adhesive carbon disks. These samples were investigated using an EVO MA 10 (Carl Zeiss, USA) SEM. SEM micrographs were taken of the longitudinal (top and bottom) sections and cross-section. At low magnification, an electron accelerating voltage of 10-20 kV and the use of a lateral secondary electron detector enabled the imaging of both fibres and the micro-porous medium with a pixel

resolution of ~670 nm in longitudinal section and ~330 nm in the cross-sectional direction.

X-ray computed tomography (X-ray CT)

A laboratory X-ray CT system, ZEISS Xradia 520 Versa (Carl Zeiss, USA) was used for 3D imaging. MEA samples were prepared as 1 mm disks, to optimise the image collection process and maximise signal-to-noise ratio. A source voltage of 40 kV and a field-of-view of ca. 0.7 mm × 0.7 mm were used for every sample. 3701 projections were captured with an exposure time of 8 s. Reconstruction of the radiographs into a 3D volume was achieved using a cone-beam filtered back projection algorithm (Reconstructor Scout-and-Scan, ZEISS) resulting in an isotropic voxel size of ~760 nm. All samples were scanned without having been run in the fuel cell.

Thermogravimetric analysis (TGA).

TGA was used to determine the Nafion and PTFE content of the gas diffusion electrode (GDE). The weight loss as a function of temperature was determined using a Pyris™ 1 TGA (PerkinElmer, USA), in a furnace with a sensitivity of 0.1 µg. The sample was heated in N₂, between 50 and 900 °C, with a heating rate of 20 °C min⁻¹ and had an initial weight of 2.29 mg.

Differential scanning calorimetry (DSC)

DSC was used to determine the Nafion membrane glass transition and melting transition temperatures. The heat flow as a function of temperature was determined by differential scanning calorimetry (DSC) using a double-furnace DSC 8000 (PerkinElmer, USA). The sample was heated in N₂, between 30 and 250 °C, with a heating rate of 20 °C min⁻¹, and had an initial weight of 5.89 mg.

Atomic force microscopy (AFM)

The AFM images of the Nafion membrane were acquired using the force tapping mode on a Bruker Icon instrument. A commercial Si tip with an anisotropic shape was used, with a nominal spring constant of 0.4 N m^{-1} , a nominal tip radius of curvature of 2 nm and nominal resonant frequency of 70 kHz (Scanasyst-air, Bruker). 2176 points per line were measured, enabling a pixel resolution of between 37 and 42 nm (for a scanned area between $82 \times 82 \mu\text{m}$ and $92 \times 92 \mu\text{m}$). The AFM parameters were manually set to minimize the pressure of tip on the membrane.

Image post-processing

For all reconstructed volumes, post-processing and image segmentation was performed using Avizo Lite® (FEI) to segment the GDL layer material, consisting of large fibres bonded with PTFE, from the micro-porous medium, catalyst medium and the Nafion polymer membrane. For each sample, a field-of-view of $300 \times 500 \mu\text{m}$ in the x - y orientation was chosen for material segmentation. The representative elementary area (REA), or minimum area above which a measurement will be representative in a larger volume [69,70], has been determined for the sample hot-pressed at $170 \text{ }^\circ\text{C}$ (Figure 2). Areas between 0.001 mm^2 and 0.15 mm^2 have been investigated using 20 samples across the material. The area above which the standard deviation is lower than 10 % is defined as the REA [69]. From the seven parameters studied (Table 1), the standard deviation is between 10 % - 50 % for samples from 0.001 mm^2 - 0.10 mm^2 , and between 2 % - 7 % above 0.10 mm^2 . Therefore, the REA is determined to be 0.10 mm^2 . As the area chosen for segmentation is 0.15 mm^2 , the subsequent analysis is statistically relevant.

The catalyst impregnated micro-porous medium, is composed of carbon / PTFE / Pt / Nafion, and is much denser than the fibres of the GDL or Nafion membrane, hence enabling threshold segmentation from the other two materials. The Nafion has

similar attenuation to the fibres, yet has a different texture, making segmentation between these two materials possible via identification and isolation of each material.

To characterise the interfacial contact between the multilayer interface, and macro-structural changes of the Nafion and MPLC, the roughness factor, and the normalised interface contact area have been defined.

The roughness factor of the material i (Nafion or MPLC) has been calculated as follows:

$$r_i = \frac{A_{i,act}}{A_g} \quad (\text{Equation 1})$$

With $A_{i,act}$ the actual surface area, and $A_{i,g}$ the geometric surface area.

The actual surface area of the gas diffusion electrode (GDE) and hot pressed membrane was determined using X-ray CT scans using the surface area volume toolkit (Avizo FEI). The actual surface area of the as-received Nafion membrane was determined using AFM. This was done by randomly sampling four 85 - 92 μm^2 spots (spot size was varied slightly only to improve tracking). $A_{Nafion,act}$ and $A_{Nafion,g}$ were calculated using the statistical quantities tool (Gwyddion). The images were spline-fit and roughness factors recalculated to account for the error in roughness factor determined by the tilt of each sample.

The normalised contact area between two surfaces was calculated as follows:

$$A_{i,j} = \frac{I_{i,j}}{A_g} \quad (\text{Equation 2})$$

With $I_{i,j}$ the contact area between material i and material j , calculated using the surface area patch modules of Avizo.

Finally, the material fraction per slice was defined as follows:

$$X_i(z) = \frac{n_i(z)}{n} \quad (\text{Equation 3})$$

With $n_i(z)$ the number of pixels segmented for material i at slice z , and n the total number of pixels in this slice which were calculated using the ImageJ software package. The materials coexistence region is defined as the length for which two or more materials are present on subsequent slices.

The material thickness and crack width has been determined by averaging over 20 measurement points across the sample.

3. Results

3.1. Characterisation of the gas diffusion electrode and Nafion membrane microstructure before assembly.

The 3D structure of the GDE has been revealed by X-ray CT, this is supported by SEM and quantification of the Nafion and PTFE content using TGA. The roughness factor of the untreated Nafion membrane was evaluated using AFM and its glass transition was determined using DSC.

The gas diffusion medium is composed of linear fibres in a planar arrangement (Figure 3a), with ~10 wt% of PTFE in the total GDE, as revealed by TGA, which shows a mass drop at 550 °C [71] (Figure 3c). The fibres structure is similar to Toray and SGL [72].

The average porosity through the medium is 70 %, calculated from the void material fraction from 3D images (Figure 3d), which is within the porosity range (30 % - 90 %)

reported for commercial GDLs measured via five different methods for PTFE contents ranging from 0 to 60 % [69].

A dense and bright phase is observed in the orthoslices (high Pt and Nafion content) (Figure 9), and a surrounding much lighter phase (MPL). However, the Pt nanoparticles (~5 nm) cannot be isolated from the surrounding carbon particles of the catalyst (~ 50 nm) due to the imaging resolution (780 nm) [30,62]. Furthermore, as the catalyst has been coated on the porous MPL, a small amount penetrates into the structure, but with a density gradient making the segmentation impossible at this resolution. Therefore, this dual layer, with a material gradient between pure MPL and pure catalyst, will subsequently be referred to as the micro-porous layer and catalyst (MPLC) and is segmented as a single material. The GDE contains 5 wt% of Nafion, as revealed by TGA with two inflection points between 300 and 400 °C (Figure 3c), characteristic of the Nafion pyrolysis [41,74–76].

The MPLC outer surface (catalyst based) has cracks with an average width of 14 μm (Table 1), which is within the same range as previously reported [30,42] (Figure 3b), and the roughness factor of the outer surface is 1.54. These cracks have formed during the formation of the micro-porous layer and the deposition of the catalyst ink, and form as the catalyst dries, in a similar way to the formation of cracks in mud. The presence of these cracks has been reported to be beneficial as they promote gas and water diffusion, without significantly reducing physical contact with the membrane [77], and can operate as an alternative to a thicker, uniform micro-porous layer with larger pores [44,46]. However, the edges may be more prone to catalyst degradation due to the higher current passed at the edges. The normalised contact area between the GDL and the MPLC is 0.4, suggesting an initially poor contact with the fibres.

AFM was used to determine the membrane roughness with higher resolution than accessible with X-ray micro-CT, which could not resolve any surface structure (Figure 4a). An average peak-valley height of 140 nm was measured (roughness factor 1.02 ± 0.02), indicating that the membrane is effectively flat on the scale of the other components. Differential scanning calorimetry reveals that the Nafion 212 has a glass transition temperature T_g at 123 °C, in the same range as that previously reported [36] (Figure 4b). A second inflection point is observed at 230 °C, which can be attributed to the melting temperature.

The range of temperatures used to study the effect of hot pressing has been selected in the context of the properties of Nafion. Hot pressing at 100 °C, corresponds to initiation of the first inflection point, 130 °C, slightly above the glass transition temperature, and 170 °C is where the second inflection point is initiated (Figure 4b). A broad temperature span has been used for the study as the physical properties Nafion vary and literature shows that hot-pressing of MEAs occurs over this range: low temperature range: 90 °C to 130 °C [2,4,36,37], intermediate range: 130 °C to 150 °C [6,8,9,38–41] and extreme range from 150 °C to 170 °C [2,4,14,15,35].

3.2. Effect of hot pressing temperature on performance and microstructure.

3.2.1. Effect of hot pressing temperature on performance.

Polarisation curves, impedance data and polarisation error bars were collected for MEAs hot pressed at 100 °C, 130 °C and 170 °C (Figure 5 a-c).

The difference in performance between the two polarisation repeats is lower than 5 mV (Fig 5 c), in the activation and ohmic region (below 600 mA cm⁻² at 100 °C and 130 °C, 450 mA cm⁻² at 170 °C), which highlights that the cell has been sufficiently broken-in [68]. The deviation in the mass transport region could be due to flooding issues, mass transport limitation, fuel starvation or material degradations.

The MEA hot pressed at 130 °C provides the highest peak power density, and lowest Ohmic resistance, with the power density 5 % and 20 % higher, and the Ohmic resistance on average 3 % and 10 % lower than the 100 °C and 170 °C cases, respectively (Fig 5 a-b).

The higher Ohmic resistance, at 100 °C and 170 °C, could be due to poorer contact between MEA layers, or a drier cell which could correlate to degradation of the Nafion membrane once hot pressed.

For MEAs hot pressed at 170 °C, the performance is much lower, with an open circuit voltage (OCV) of 0.82 V and a limiting current density of 625 mA cm⁻² (cf. 0.91 V and 755 mA cm⁻² for MEA at 130 °C) (Fig 5 a). The lower OCV is indicative of hydrogen crossover caused by pinholes and / or electrolyte thinning [78]. The higher Ohmic resistance may be a result of membrane damage and the mass transport limitation is consistent with disruption of the pore network structure, impeding gas access to the catalyst. For the MEAs hot pressed at 100 °C, the lower voltage in the charge transfer region may suggest lack of electrical contact; however, the limiting current density is identical to the one at 130 °C, suggesting that the mass transport behaviour is unaffected by the lower hot pressing temperature.

However, these assumptions cannot be validated without further evaluation of the MEA microstructure, to analyse the multilayer interfaces (GDL/MPLC, Nafion/GDL and Nafion/MPLC).

3.2.2. Effect of hot pressing temperature on MEA microstructure

As the same GDE material has been used on both sides of the Nafion membrane, only the bottom half of the MEA (as shown) has been segmented. For every sample, a full 3D volume rendering of the unsegment structure is shown to aid image correlation. To the authors' knowledge, this is the first time X-ray CT has been used to segment Nafion from the catalyst/MPL and the GDL fibres after hot-pressing in polymer electrolyte fuel cells. Table 1 describes the changes of normalised contact area, thickness, roughness factors, and width of the surface cracks over the four samples. The effect of hot pressing at 100 °C, 130 °C and 170 °C can be seen in Figure 6, Figure 7 and Figure 8, respectively. These effects, and microstructural changes are discussed in the following section.

Considering the 100 °C hot pressed MEA first (Figure 6), it can be seen that partial bonding has occurred between the Nafion and MPLC, as gaps in the interface are visible in the volume rendering and the fully segmented structure (Figure 6 a-b).

Further examination shows that the surface of the MPLC has slightly smaller cracks (Figure 6c) than before hot pressing (Figure 3a), with a reduction in average crack width from 14 μm to 12 μm (Table 1). Furthermore, the thickness of the membrane has been reduced by hot pressing from 50.8 μm to 44 μm , but remains completely intact with no sign of pin-hole formation. The membrane and catalyst surface have 'sharp' edges, and clean cracks are seen in the MPLC. This could be linked to 100 °C being below the glass transition temperature of Nafion, resulting in more of a mechanical pressing (stamping) effect than the 'flowing' of Nafion between the phases. The Nafion roughness factor has increased from 1.02 to 1.15, whereas the

MPLC outer roughness factor has reduced from 1.54 to 1.26 (Table 1). Altogether, this suggests that hot pressing at 100 °C is not high enough to adequately bond the Nafion and the MPLC, resulting in a normalised contact area of only 0.59. This effect is particularly visible on the X-ray orthoslices in Figure 9a, where the MPLC is only partially in contact with the Nafion membrane. The partial bonding of the MPLC and the Nafion is consistent with the higher Ohmic resistance compared to the 130 °C case. As revealed in the material solid fraction profile, and the interfacial contact, there is no sign of fibres from the GDL penetrating through the MPL to the membrane (Figure 6e, Table 1), with distinct regions for all materials clearly visible. No visible deformation onto the carbon fibres has been caused (Figure 6d), in comparison with Figure 3a.

When the cell is hot pressed at 130 °C (Figure 7), notable microstructural changes are observed on the Nafion membrane surface, and the MPLC surface (Figure 7b-c), while the volume rendering (Figure 7 a) shows a more compact structure in comparison to 100 °C. Firstly, the presence of locally inflated areas can be seen in the Nafion surface (Figure 7 b), with an increase of the roughness factor to 1.33, whereas the roughness of the MPLC outer surface has reduced to 1.32 (Table 1). Furthermore, the normalised contact area $A_{MPLC/Nafion}$ has increased from 0.62 to 1.28, highlighting that the bonding process between the Nafion ionomer contained in the MPLC (5 %) and the Nafion membrane is better than the 100 °C case, with the same roughness for both materials indicating optimal conditions for bonding. This is supported by Figure 9b, with optimum contact between the Nafion membrane and the MPLC. Finally, a few fibres have ruptured, along the largest diagonal MPLC crack, possibly caused by the bounding process (Figure 7 c-d).

The normalised contact area of 1.28 reveals not only surface contact, but also Nafion intrusion into the cracks of the MPLC, as supported by the 40 µm coexistence region (Figure 7e).

Altogether, this shows that hot pressing above the glass transition temperature significantly changes the MEA structure. The transition from glass to rubber allows Nafion to flow into adjacent phases, which explains why the MPLC appears to have been 'pushed' onto the fibres (Figure 7b-c). Furthermore, more facile lateral movement of the MPLC during hot pressing results in closure of the cracks which have healed and reduced in width from 12 μm to 7 μm . Another effect of the Nafion expansion is a change of material fraction of increasing from 17 % to 22 % (Figure 7e). An explanation could be that as Nafion expands, it adds additional pressure on the GDL, in addition to the initial load in the hot press, leading to further compression. A small quantity of Nafion has slightly intruded into the GDL ($\sim 25 \mu\text{m}$) through the MPLC cracks (Figure 7e), with an interfacial contact between the Nafion and the GDL of 2.1×10^{-3} .

The results at 100 °C and 130 °C are consistent with the SEM study of Martiemianov *et al.* [36] using Nafion 112. However, the utilisation of X-ray CT enables quantification of the phase contact area and volumetric distribution within the structure of the MEA.

Although the normalised contact area between the Nafion and the MPLC is 55 % lower at 100 °C than 130 °C, the electrochemical performance is not significantly affected in comparison. One explanation could be that further contact is created when the fuel cell is compressed within the cell assembly during operation.

Finally, hot pressing was performed at 170 °C (Figure 8). The volume rendering shows Nafion intrusion in the GDL and MPLC (Figure 8a), and interfacial damage, with acute thinning. Although Nafion can be handled up to 175 °C [79], extensive deformations can be observed on the segmented Nafion membrane surface (Figure

8b, Figure 9c), leading to a roughness factor of 2.98 (Table 1). Increased mobility of Nafion at this higher temperature has deformed its structure, and ruptured the MPLC, forming large cracks (average size: 13 μm) (Figure 8c). The membrane and MPLC have propagated into the GDL, with a large intrusion of the Nafion into GDL of 120 μm (Figure 8e, Figure 9c). The dashed area in Figure 9c highlights an area where the Nafion has deformed the MPLC, penetrated through the MPLC into the GDL, with the highly attenuating Pt in the catalyst layer (white) clearly visible at a significant depth into the GDL. As a result of the Nafion intrusion, the normalised contact area between the GDL and the MPLC has reduced to 0.76, as it has weakened the MPLC/GDL interface. Whereas the normalised contact area between the GDL and Nafion has increased by two orders of magnitude in comparison with hot pressing at 130 °C. Finally, the carbon fibres (Figure 8d) have numerous rupture points at the surface of the sample, possibly caused by the extensive deformations.

As the Nafion deformed the MPLC, the MPLC roughness factor has increased to 1.48, with a normalised contact area of 1.45 (Table 1). Some of the cracks in the MPLC are likely to have been present before hot-pressing; however, small localised cracks parallel and perpendicular to the fibres' orientation suggest that these have been created by the large pressure caused by the expansion of the Nafion membrane. Alternatively, the high temperature may make the (Nafion containing) MPLC more pliable, enabling the GDL to penetrate further, leading to the formation of cracks in the cooling phase.

It can be seen that the Nafion membrane exhibits several pinholes (Figure 8b), as the Nafion diffuses through the path of least resistance via the cracks (pre and post hot pressing) in the MPLC. These pinholes cover 2 % of the segmented area and the electrolyte has seen extensive thinning. The Nafion is likely to have diffused through

parts of the MPLC that are locally weaker, creating a preferential pathway of least resistance for large amounts of material, leading to localised pinholes.

This provides an explanation for the much lower OCV observed on the polarisation curve, as these pinholes will lead to gas crossover. This has also been reported to lead to further performance degradation over long-term operation [78]. The large mass transport limitations at high current density also shows that the MEA structure has been compromised and access of gas to the catalyst impeded by the flow of Nafion disrupting the MPLC structure and filling pores in the GDL.

4. Conclusion

In this study, the effect of hot pressing for three samples with identical load, yet three different hot pressing temperatures has been highlighted. The cell hot pressed at 130 °C exhibits best performance, yet also shows the optimum contact between the catalyst layer and Nafion membrane. In comparison, hot pressing at 100 °C creates a non-ideal interfacial bond, with poor contact between the catalyst and the membrane; whereas hot pressing at 170 °C leads to membrane delamination, pin-hole formation and gas crossover.

Correlation of 3D microstructural characterisation with electrochemical performance has revealed new insight into the process of MEA fabrication as a function of temperature. The MEA materials have been chosen to be as generic as possible and the trends observed are likely to hold across a reasonable range of materials. However, changing materials' properties and thickness will directly influence the results. For instance, a thicker catalyst layer with initially smaller cracks, may resist

Nafion intrusion at higher temperatures of 170 °C and not tear apart. Similarly, a thicker membrane may not necessarily create pinholes. In addition, the porosity of the GDL may also affect this process, as a less porous GDL may resist intrusion and provide stronger backbone strength to the MPLC. Finally, a higher GDL PTFE content has been linked with resistance to deformation under compression, and could retain the fibres' integrity while the cell is hot pressed at higher temperatures. It is therefore recommended that a systematic study is performed using combined X-ray CT and electrochemical testing to optimise new MEA materials' combinations.

5. Acknowledgements

The authors would like to acknowledge the EPSRC for supporting the Electrochemical Innovation Lab through (EP/M009394/1, EP/G030995/1, EP/I037024/1, EP/M014371/1 and EP/M023508/1). PRS acknowledges funding from the Royal Academy of Engineering. We thank Dr. Han Wu and the EPSRC CNIE research facility service (EPSRC Award, EP/K038656/1) at University College London for the collection of the TGA/DSC data.

6. References

- [1] E.A. Ticianelli, C.R. Derouin, A. Redondo, S. Srinivasan, Methods to Advance Technology of Proton Exchange Membrane Fuel Cells, *J. Electrochem. Soc.* 135 (1988) 2209–2214. doi:10.1149/1.2096240.
- [2] J.C. Lin, C.M. Lai, F.P. Ting, S.D. Chyou, K.L. Hsueh, Influence of hot-pressing temperature on the performance of PEMFC and catalytic activity, *J. Appl. Electrochem.* 39 (2009) 1067–1073. doi:10.1007/s10800-008-9758-1.
- [3] O. Okur, Ç. Iyigün Karadağ, F.G. Boyacı San, E. Okumuş, G. Behmenyar, Optimization of parameters for hot-pressing manufacture of membrane electrode assembly for PEM (polymer electrolyte membrane fuel cells) fuel cell, *Energy*. 57 (2013) 574–580. doi:10.1016/j.energy.2013.05.001.
- [4] A. Therdthianwong, P. Manomayidthikarn, S. Therdthianwong, Investigation of membrane electrode assembly (MEA) hot-pressing parameters for proton exchange membrane fuel cell, *Energy*. 32 (2007) 2401–2411. doi:10.1016/j.energy.2007.07.005.

- [5] I.A. Schneider, D. Kramer, A. Wokaun, G.G. Scherer, Spatially resolved characterization of PEFCs using simultaneously neutron radiography and locally resolved impedance spectroscopy, *Electrochem. Commun.* 7 (2005) 1393–1397. doi:10.1016/j.elecom.2005.09.017.
- [6] M. Prasanna, E.A. Cho, T.H. Lim, I.H. Oh, Effects of MEA fabrication method on durability of polymer electrolyte membrane fuel cells, *Electrochim. Acta.* 53 (2008) 5434–5441. doi:10.1016/j.electacta.2008.02.068.
- [7] S.U. Jeong, E.A. Cho, H.-J. Kim, T.-H. Lim, I.-H. Oh, S.H. Kim, Effects of cathode open area and relative humidity on the performance of air-breathing polymer electrolyte membrane fuel cells, *J. Power Sources.* 158 (2006) 348–353. doi:10.1016/j.jpowsour.2005.09.044.
- [8] D. DeBonis, M. Mayer, A. Omoobi, R.S. Besser, Analysis of mechanism of Nafion® conductivity change due to hot pressing treatment, *Renew. Energy.* 89 (2016) 200–206. doi:10.1016/j.renene.2015.11.081.
- [9] H.A. Gasteiger, S.S. Kocha, B. Sompalli, F.T. Wagner, Activity benchmarks and requirements for Pt, Pt-alloy, and non-Pt oxygen reduction catalysts for PEMFCs, *Appl. Catal. B Environ.* 56 (2005) 9–35. doi:10.1016/j.apcatb.2004.06.021.
- [10] J.J. Hwnag, W.R. Chang, R.G. Peng, P.Y. Chen, A. Su, Experimental and numerical studies of local current mapping on a PEM fuel cell, *Int. J. Hydrogen Energy.* 33 (2008) 5718–5727. doi:10.1016/j.ijhydene.2008.07.035.
- [11] H. Tang, S. Wang, S.P. Jiang, M. Pan, A comparative study of CCM and hot-pressed MEAs for PEM fuel cells, *J. Power Sources.* 170 (2007) 140–144. doi:10.1016/j.jpowsour.2007.03.062.
- [12] E. Gulzow, C. Wieser, A. Helmbold, A new technique for two-dimensional current distribution measurements in electrochemical cells, *J. Appl. Electrochem.* 30 (2000) 803–807.
- [13] L. Xing, X. Liu, T. Alaje, R. Kumar, M. Mamlouk, K. Scott, A two-phase flow and non-isothermal agglomerate model for a proton exchange membrane (PEM) fuel cell, *Energy.* 73 (2014) 618–634. doi:10.1016/j.energy.2014.06.065.
- [14] E. Engebretsen, J.B. Robinson, O. Obeisun, T. Mason, D. Finegan, G. Hinds, et al., Electro-thermal impedance spectroscopy applied to an open-cathode polymer electrolyte fuel cell, *J. Power Sources.* 302 (2016) 210–214. doi:10.1016/j.jpowsour.2015.10.047.
- [15] O. Obeisun, Q. Meyer, J. Robinson, C.W. Gibbs, A.R. Kucernak, P.R. Shearing, et al., Development of open-cathode polymer electrolyte fuel cells using printed circuit board flow-field plates: Flow geometry characterisation, *Int. J. Hydrogen Energy.* 39 (2014) 18326–18336. doi:10.1016/j.ijhydene.2014.08.106.
- [16] S.M. Andersen, R. Dhiman, M.J. Larsen, E. Skou, Importance of electrode hot-pressing conditions for the catalyst performance of proton exchange membrane fuel cells, *Appl. Catal. B Environ.* 172–173 (2015) 82–90. doi:10.1016/j.apcatb.2015.02.023.
- [17] M.W. Reed, R.J. Brodd, Porous Carbon for Fuel Cell Electrodes, *Carbon N. Y.* 3 (1965) 241–246.
- [18] U. Pasaogullari, C.Y. Wang, Liquid Water Transport in Gas Diffusion Layer of Polymer Electrolyte Fuel Cells, *J. Electrochem. Soc.* 151 (2004) A399. doi:10.1149/1.1646148.
- [19] O.S. Burheim, J.G. Pharoah, H. Lampert, P.J.S. Vie, S. Kjelstrup, Through-

- Plane Thermal Conductivity of PEMFC Porous Transport Layers, *J. Fuel Cell Sci. Technol.* 8 (2011) 21013. doi:10.1115/1.4002403.
- [20] J.P. James, H.-W. Choi, J.G. Pharoah, X-ray computed tomography reconstruction and analysis of polymer electrolyte membrane fuel cell porous transport layers, *Int. J. Hydrogen Energy.* 37 (2012) 18216–18230. doi:10.1016/j.ijhydene.2012.08.077.
- [21] J.-C. Tsai, C.-K. Lin, Effect of PTFE content in gas diffusion layer based on Nafion®/PTFE membrane for low humidity proton exchange membrane fuel cell, *J. Taiwan Inst. Chem. Eng.* 42 (2011) 945–951. doi:10.1016/j.jtice.2011.05.008.
- [22] M.V. Williams, E. Begg, L. Bonville, H.R. Kunz, J.M. Fenton, Characterization of Gas Diffusion Layers for PEMFC, *J. Electrochem. Soc.* 151 (2004) A1173–1180. doi:10.1149/1.1764779.
- [23] H. Li, Y. Tang, Z. Wang, Z. Shi, S. Wu, D. Song, et al., A review of water flooding issues in the proton exchange membrane fuel cell, *J. Power Sources.* 178 (2008) 103–117. doi:10.1016/j.jpowsour.2007.12.068.
- [24] S. Park, J.-W. Lee, B.N. Popov, A review of gas diffusion layer in PEM fuel cells: Materials and designs, *Int. J. Hydrogen Energy.* 37 (2012) 5850–5865. doi:10.1016/j.ijhydene.2011.12.148.
- [25] A.Z. Weber, J. Newman, Effects of Microporous Layers in Polymer Electrolyte Fuel Cells, *J. Electrochem. Soc.* 152 (2005) A677. doi:10.1149/1.1861194.
- [26] M.S. Wilson, J.A. Valerio, S. Gottesfeld, Low platinum loading for polymer electrolyte fuel cells fabricated using thermoplastic ionomers, *Electrochim. Acta.* 40 (1995) 355–363. doi:10.1016/0013-4686(94)00272-3.
- [27] A. Suzuki, T. Hattori, R. Miura, H. Tsuboi, N. Hatakeyama, H. Takaba, et al., Porosity and Pt content in the catalyst layer of PEMFC: Effects on diffusion and polarization characteristics, *Int. J. Electrochem. Sci.* 5 (2010) 1948–1961.
- [28] N. Mansor, A. Belen Jorge, F. Corà, C. Gibbs, R. Jervis, P.F. McMillan, et al., Development of Graphitic-Carbon Nitride Materials as Catalyst Supports for Polymer Electrolyte Fuel Cells, *ECS Trans.* 58 (2013) 1767–1778. doi:10.1149/05801.1767ecst.
- [29] N. Mansor, A.B. Jorge, F. Corà, C. Gibbs, R. Jervis, P.F. McMillan, et al., Graphitic Carbon Nitride Supported Catalysts for Polymer Electrolyte Fuel Cells, *J. Phys. Chem. C.* 118 (2014) 6831–6838. doi:10.1021/jp412501j.
- [30] A. Pokhrel, M. El Hannach, F.P. Orfino, M. Dutta, E. Kjeang, Failure analysis of fuel cell electrodes using three-dimensional multi-length scale X-ray computed tomography, *J. Power Sources.* 329 (2016) 330–338. doi:10.1016/j.jpowsour.2016.08.092.
- [31] M. Wilson, S. Gottesfeld, Thin-film catalyst layers for polymer electrolyte fuel cell electrodes, *J. Appl. Electrochem.* 22 (1992) 1–7. doi:10.1007/BF01093004.
- [32] H.R.Q. Jhong, F.R. Brushett, P.J.A. Kenis, The effects of catalyst layer deposition methodology on electrode performance, *Adv. Energy Mater.* 3 (2013) 589–599. doi:10.1002/aenm.201200759.
- [33] A.T. Haug, R.E. White, J.W. Weidner, W. Huang, S. Shi, T. Stoner, et al., Increasing Proton Exchange Membrane Fuel Cell Catalyst Effectiveness Through Sputter Deposition, *J. Electrochem. Soc.* 149 (2002) A280. doi:10.1149/1.1446082.
- [34] A. Strong, C. Thornberry, S. Beattie, R. Chen, S.R. Coles, Depositing Catalyst

- Layers in Polymer Electrolyte Membrane Fuel Cells: A Review, *J. Fuel Cell Sci. Technol.* 12 (2015) 64001. doi:10.1115/1.4031961.
- [35] N. Wagner, E. Gülzow, Change of electrochemical impedance spectra (EIS) with time during CO-poisoning of the Pt-anode in a membrane fuel cell, *J. Power Sources.* 127 (2004) 341–347. doi:10.1016/j.jpowsour.2003.09.031.
- [36] S. Martemianov, V.A. Raileanu Ilie, C. Coutanceau, Improvement of the proton exchange membrane fuel cell performances by optimization of the hot pressing process for membrane electrode assembly, *J. Solid State Electrochem.* 18 (2014) 1261–1269. doi:10.1007/s10008-013-2273-2.
- [37] K. Teranishi, S. Tsushima, S. Hirai, Study of the Effect of Membrane Thickness on the Performance of Polymer Electrolyte Fuel Cells by Water Distribution in a Membrane, *Electrochem. Solid-State Lett.* 8 (2005) A281. doi:10.1149/1.1897343.
- [38] G. Li, P.G. Pickup, Measurement of single electrode potentials and impedances in hydrogen and direct methanol PEM fuel cells, *Electrochim. Acta.* 49 (2004) 4119–4126. doi:10.1016/j.electacta.2004.04.005.
- [39] E. Passalacqua, F. Lufrano, G. Squadrito, Nafion content in the catalyst layer of polymer electrolyte fuel cells: effects on structure and performance, *Electrochim.* 46 (2001) 799–805.
- [40] J. Wu, S. Galli, I. Lagana, A. Pozio, G. Monteleone, X. Zi, et al., An air-cooled proton exchange membrane fuel cell with combined oxidant and coolant flow, *J. Power Sources.* 188 (2009) 199–204. doi:10.1016/j.jpowsour.2008.11.078.
- [41] Y. Devrim, A. Albostan, Enhancement of PEM fuel cell performance at higher temperatures and lower humidities by high performance membrane electrode assembly based on Nafion/zeolite membrane, *Int. J. Hydrogen Energy.* 40 (2015) 15328–15335. doi:10.1016/j.ijhydene.2015.02.078.
- [42] T. Sasabe, P. Deevanhxay, S. Tsushima, S. Hirai, Soft X-ray visualization of the liquid water transport within the cracks of micro porous layer in PEMFC, *Electrochem. Commun.* 13 (2011) 638–641. doi:10.1016/j.elecom.2011.03.033.
- [43] J. Yu, M.N. Islam, T. Matsuura, M. Tamano, Y. Hayashi, M. Hori, Improving the Performance of a PEMFC with Ketjenblack EC-600JD Carbon Black as the Material of the Microporous Layer, *Electrochem. Solid-State Lett.* 8 (2005) A320–A323. doi:10.1149/1.1904504.
- [44] Q. Meyer, S. Ashton, P. Boillat, M. Cochet, E. Engebretsen, D.P. Finegan, et al., Effect of gas diffusion layer properties on water distribution across air-cooled, open-cathode polymer electrolyte fuel cells: A combined ex-situ X-ray tomography and in-operando neutron imaging study, *Electrochim. Acta.* 211 (2016) 478–487. doi:10.1016/j.electacta.2016.06.068.
- [45] I. V. Zenyuk, P.K. Das, A.Z. Weber, Understanding Impacts of Catalyst-Layer Thickness on Fuel-Cell Performance via Mathematical Modeling, *J. Electrochem. Soc.* 163 (2016) F691–F703. doi:10.1149/2.1161607jes.
- [46] H. Ostadi, P. Rama, Y. Liu, R. Chen, X.X. Zhang, K. Jiang, 3D reconstruction of a gas diffusion layer and a microporous layer, *J. Memb. Sci.* 351 (2010) 69–74. doi:10.1016/j.memsci.2010.01.031.
- [47] S.J. Osborn, M.K. Hassan, G.M. Divoux, D.W. Rhoades, K.A. Mauritz, R.B. Moore, Glass transition temperature of perfluorosulfonic acid ionomers, *Macromolecules.* 40 (2007) 3886–3890. doi:10.1021/ma062029e.
- [48] S. Yu, D. Jung, Thermal management strategy for a proton exchange

- membrane fuel cell system with a large active cell area, *Renew. Energy*. 33 (2008) 2540–2548. doi:10.1016/j.renene.2008.02.015.
- [49] A.M. Chaparro, B. Gallardo, M.A. Folgado, A.J. Martín, L. Daza, PEMFC electrode preparation by electrospray: Optimization of catalyst load and ionomer content, *Catal. Today*. 143 (2009) 237–241. doi:10.1016/j.cattod.2008.12.003.
- [50] S. Litster, G. McLean, PEM fuel cell electrodes, *J. Power Sources*. 130 (2004) 61–76. doi:10.1016/j.jpowsour.2003.12.055.
- [51] E. Antolini, L. Giorgi, a. Pozio, E. Passalacqua, Influence of Nafion loading in the catalyst layer of gas-diffusion electrodes for PEFC, *J. Power Sources*. 77 (1999) 136–142. doi:10.1016/S0378-7753(98)00186-4.
- [52] Y. Tang, J. Zhang, C. Song, H. Liu, J. Zhang, H. Wang, et al., Temperature Dependent Performance and In Situ AC Impedance of High-Temperature PEM Fuel Cells Using the Nafion-112 Membrane, *J. Electrochem. Soc.* 153 (2006) A2036–A2043. doi:10.1149/1.2337008.
- [53] D. Gerteisen, T. Heilmann, C. Ziegler, Modeling the phenomena of dehydration and flooding of a polymer electrolyte membrane fuel cell, *J. Power Sources*. 187 (2009) 165–181. doi:10.1016/j.jpowsour.2008.10.102.
- [54] R.A. Silva, T. Hashimoto, G.E. Thompson, C.M. Rangel, Characterization of MEA degradation for an open air cathode PEM fuel cell, *Int. J. Hydrogen Energy*. 37 (2012) 7299–7308. doi:10.1016/j.ijhydene.2011.12.110.
- [55] T.J. Mason, J. Millichamp, T.P. Neville, A. El-kharouf, B.G. Pollet, D.J.L. Brett, Effect of clamping pressure on ohmic resistance and compression of gas diffusion layers for polymer electrolyte fuel cells, *J. Power Sources*. 219 (2012) 52–59. doi:10.1016/j.jpowsour.2012.07.021.
- [56] S. Odaya, R.K. Phillips, Y. Sharma, J. Bellerive, A.B. Phillion, M. Hoorfar, Electrochimica Acta X-ray Tomographic Analysis of Porosity Distributions in Gas Diffusion Layers of Proton Exchange Membrane Fuel Cells, *Electrochim. Acta*. 152 (2015) 464–472. doi:10.1016/j.electacta.2014.11.143.
- [57] J. Yu, Z. Jiang, M. Hou, D. Liang, Y. Xiao, M. Dou, et al., Analysis of the behavior and degradation in proton exchange membrane fuel cells with a dead-ended anode, *J. Power Sources*. 246 (2014) 90–94. doi:10.1016/j.jpowsour.2013.06.163.
- [58] H. Ito, T. Iwamura, S. Someya, T. Munakata, A. Nakano, Y. Heo, et al., Effect of through-plane polytetrafluoroethylene distribution in gas diffusion layers on performance of proton exchange membrane fuel cells, *J. Power Sources*. 306 (2016) 289–299. doi:10.1016/j.jpowsour.2015.12.020.
- [59] A. Pfrang, D. Veyret, F. Sieker, G. Tsotridis, X-ray computed tomography of gas diffusion layers of PEM fuel cells: Calculation of thermal conductivity, *Int. J. Hydrogen Energy*. 35 (2010) 3751–3757. doi:10.1016/j.ijhydene.2010.01.085.
- [60] F.E. Hızir, S.O. Ural, E.C. Kumbur, M.M. Mench, Characterization of interfacial morphology in polymer electrolyte fuel cells: Micro-porous layer and catalyst layer surfaces, *J. Power Sources*. 195 (2010) 3463–3471. doi:10.1016/j.jpowsour.2009.11.032.
- [61] S. Thiele, R. Zengerle, C. Ziegler, Nano-morphology of a polymer electrolyte fuel cell catalyst layer-imaging, reconstruction and analysis, *Nano Res.* 4 (2011) 849–860. doi:10.1007/s12274-011-0141-x.
- [62] S. Thiele, T. Fürstehaupt, D. Banham, T. Hutzenlaub, V. Birss, C. Ziegler, et

- al., Multiscale tomography of nanoporous carbon-supported noble metal catalyst layers, *J. Power Sources*. 228 (2013) 185–192. doi:10.1016/j.jpowsour.2012.11.106.
- [63] S. Vierrath, F. Güder, A. Menzel, M. Hagner, R. Zengerle, M. Zacharias, et al., Enhancing the quality of the tomography of nanoporous materials for better understanding of polymer electrolyte fuel cell materials, *J. Power Sources*. 285 (2015) 413–417. doi:10.1016/j.jpowsour.2015.03.110.
- [64] H. Ostadi, P. Rama, Y. Liu, R. Chen, X.X. Zhang, K. Jiang, Influence of threshold variation on determining the properties of a polymer electrolyte fuel cell gas diffusion layer in X-ray nano-tomography, *Chem. Eng. Sci.* 65 (2010) 2213–2217. doi:10.1016/j.ces.2009.12.019.
- [65] S. Odaya, R.K. Phillips, Y. Sharma, J. Bellerive, a. B. Phillion, M. Hoorfar, X-ray Tomographic Analysis of Porosity Distributions in Gas Diffusion Layers of Proton Exchange Membrane Fuel Cells, *Electrochim. Acta*. 152 (2015) 464–472. doi:10.1016/j.electacta.2014.11.143.
- [66] T. Koido, T. Furusawa, K. Moriyama, An approach to modeling two-phase transport in the gas diffusion layer of a proton exchange membrane fuel cell, *J. Power Sources*. 175 (2008) 127–136. doi:10.1016/j.jpowsour.2007.09.029.
- [67] A. Pfrang, S. Didas, G. Tsotridis, X-ray computed tomography of gas diffusion layers of PEM fuel cells: Segmentation of the microporous layer, *J. Power Sources*. 235 (2013) 81–86. doi:10.1016/j.jpowsour.2013.01.179.
- [68] Membrane Electrode Assembly (MEA) Activation Procedures, (n.d.). <http://fuelcellsetc.com/2013/04/membrane-electrode-assembly-mea-activation-procedures/> (accessed May 4, 2017).
- [69] J. Roth, J. Eller, F. Marone, F.N. Bu, Investigation of the Representative Area of the Water Saturation in Gas Diffusion Layers of Polymer Electrolyte Fuel Cells, *J. Phys. Chem. C*. 117 (2013) 25991–25999. doi:10.1021/jp4057169.
- [70] O.O. Taiwo, D.P. Finegan, D.S. Eastwood, J.L. Fife, L.D. Brown, J.A. Darr, et al., Comparison of three-dimensional analysis and stereological techniques for quantifying lithium-ion battery electrode microstructures, *J. Microsc.* 263 (2016) 280–292. doi:10.1111/jmi.12389.
- [71] S. Yu, X. Li, J. Li, S. Liu, W. Lu, Z. Shao, et al., Study on hydrophobicity degradation of gas diffusion layer in proton exchange membrane fuel cells, *Energy Convers. Manag.* 76 (2013) 301–306. doi:10.1016/j.enconman.2013.07.034.
- [72] R.R. Rashapov, J. Unno, J.T. Gostick, Characterization of PEMFC Gas Diffusion Layer Porosity, *J. Electrochem. Soc.* 162 (2015) F603–F612. doi:10.1149/2.0921506jes.
- [73] E.C.S. Transactions, T.E. Society, Heterogeneous Porosity Distribution under Compression Condition of Gas Diffusion Layer Using Synchrotron X-Ray Tomography Junho Je, 50 (2012) 369–374.
- [74] S.H. de Almeida, Y. Kawano, Thermal Behavior of Nafion Membrane, *J. Therm. Anal. Calorim.* 58 (1999) 569–577. doi:10.1023/A:1010196226309.
- [75] a. K. Sahu, S. Meenakshi, S.D. Bhat, a. Shahid, P. Sridhar, S. Pitchumani, et al., Meso-Structured Silica-Nafion Hybrid Membranes for Direct Methanol Fuel Cells, *J. Electrochem. Soc.* 159 (2012) F702–F710. doi:10.1149/2.036211jes.
- [76] Q. Deng, C.A. Wilkie, R.B. Moore, K.A. Mauritz, TGA–FTi.r. investigation of the thermal degradation of Nafion® and Nafion®/[silicon oxide]-based nanocomposites, *Polymer (Guildf)*. 39 (1998) 5961–5972. doi:10.1016/S0032-

- 3861(98)00055-X.
- [77] S.M. Kim, C.-Y. Ahn, Y.-H. Cho, S. Kim, W. Hwang, S. Jang, et al., High-performance Fuel Cell with Stretched Catalyst-Coated Membrane: One-step Formation of Cracked Electrode, *Sci. Rep.* 6 (2016) 26503. doi:10.1038/srep26503.
 - [78] A.Z. Weber, Gas-Crossover and Membrane-Pinhole Effects in Polymer-Electrolyte Fuel Cells, *J. Electrochem. Soc.* 155 (2008) B521. doi:10.1149/1.2898130.
 - [79] Nafion Ion Exchange Materials Safety in Handling and Use, *Tech. Bull. T-01.* (n.d.). https://www.chemours.com/Nafion/en_US/assets/downloads/nafion-safety-handling-technical-information.pdf (accessed October 3, 2016).

List of figures

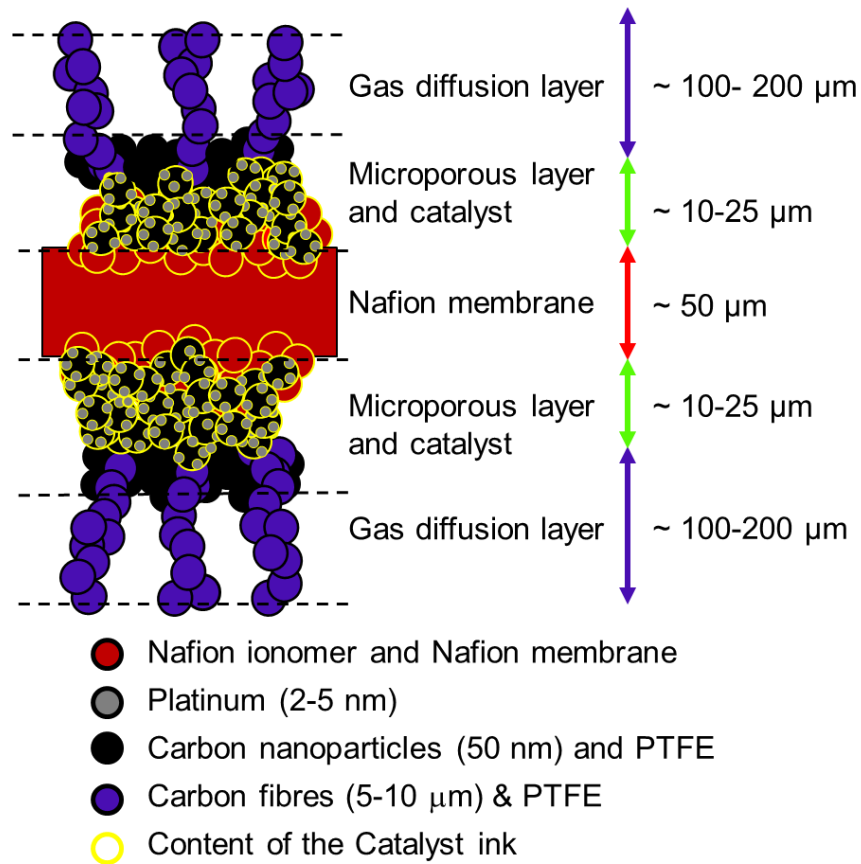


Figure 1. Schematic of the MEA showing the distributed interface between different components and their typical thicknesses.

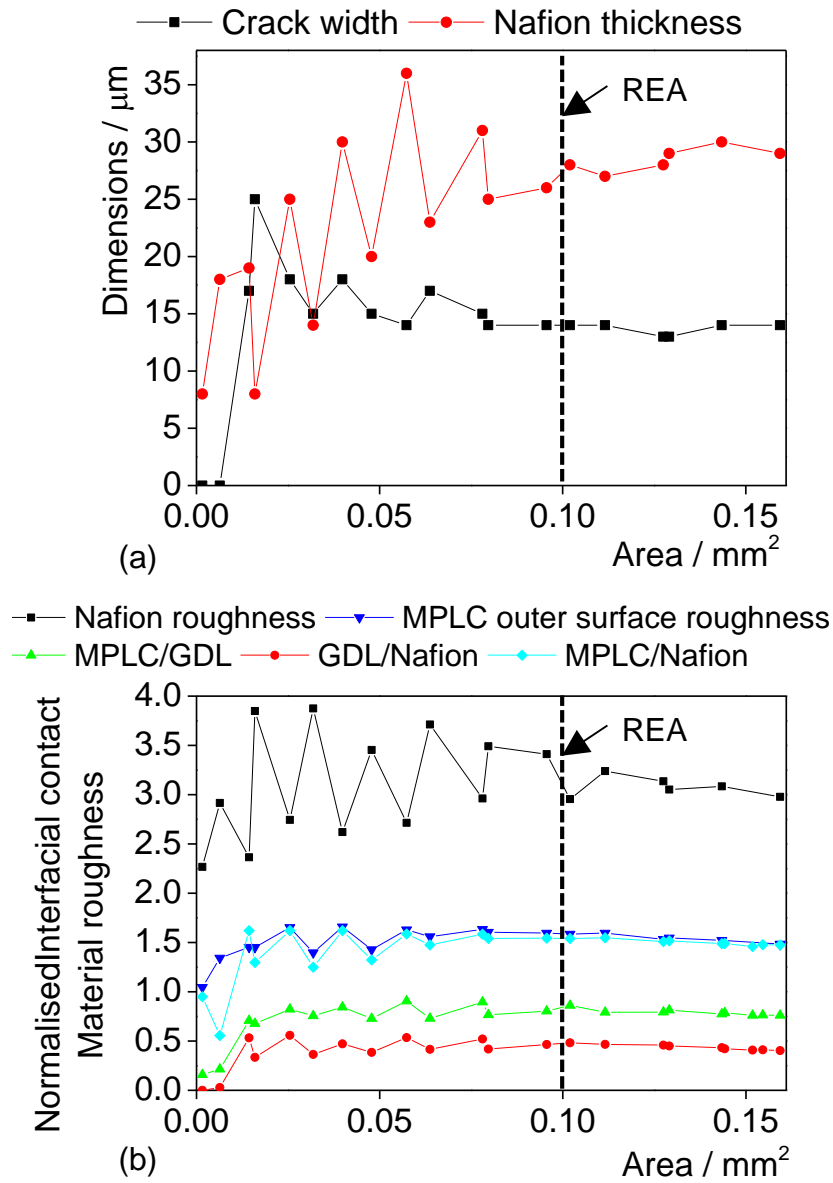


Figure 2. Determination of the representative elementary area for the sample hot pressed at $170 \text{ }^\circ\text{C}$ for the seven interfacial and morphological variables. The dash line has been added to highlight the change of standard deviation before / after the REA.

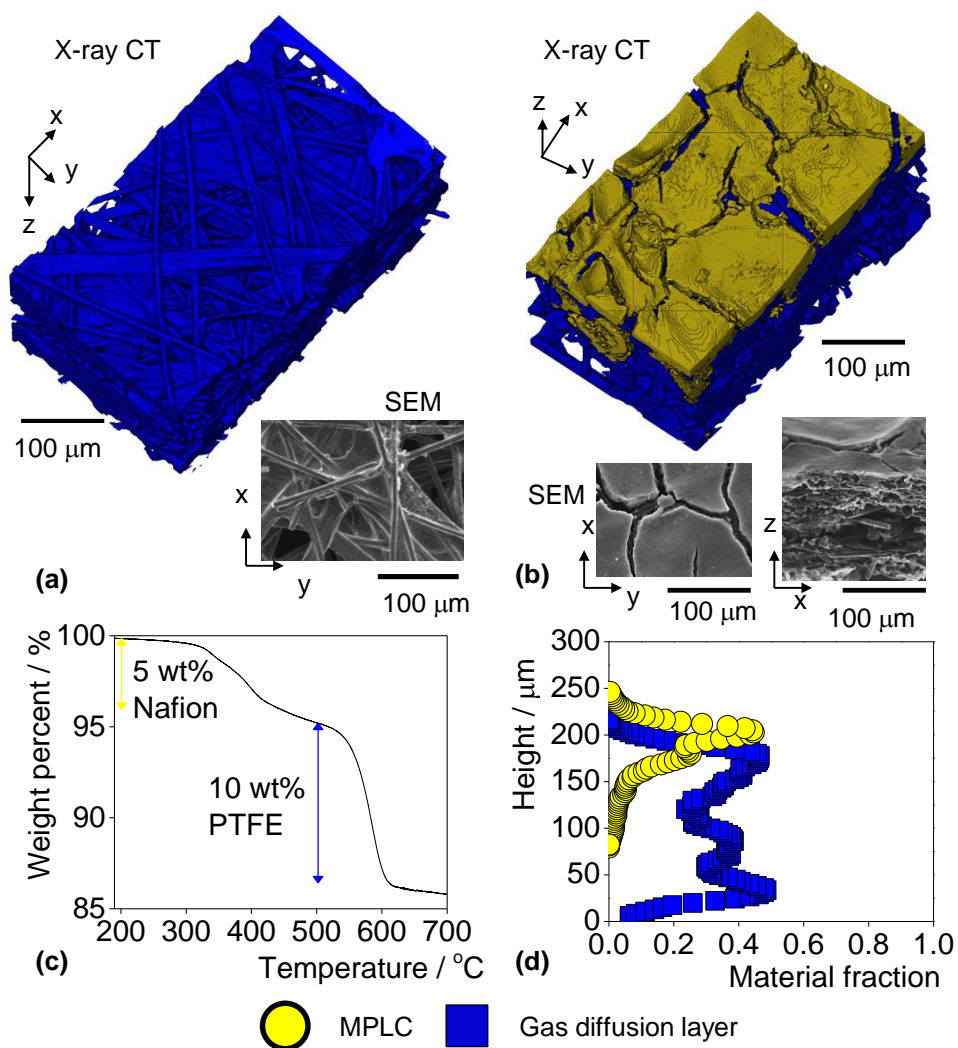


Figure 3. Characterisation of the gas diffusion layer coated with micro-porous layer and catalyst medium (MPLC). (a) X-ray CT and SEM, longitudinal section, of the GDL uncoated side; (b) X-ray CT and SEM, in longitudinal and cross-section, of the MPLC and GDL; (c) TGA of the GDE; (d) material fraction of the MPLC and GDL.

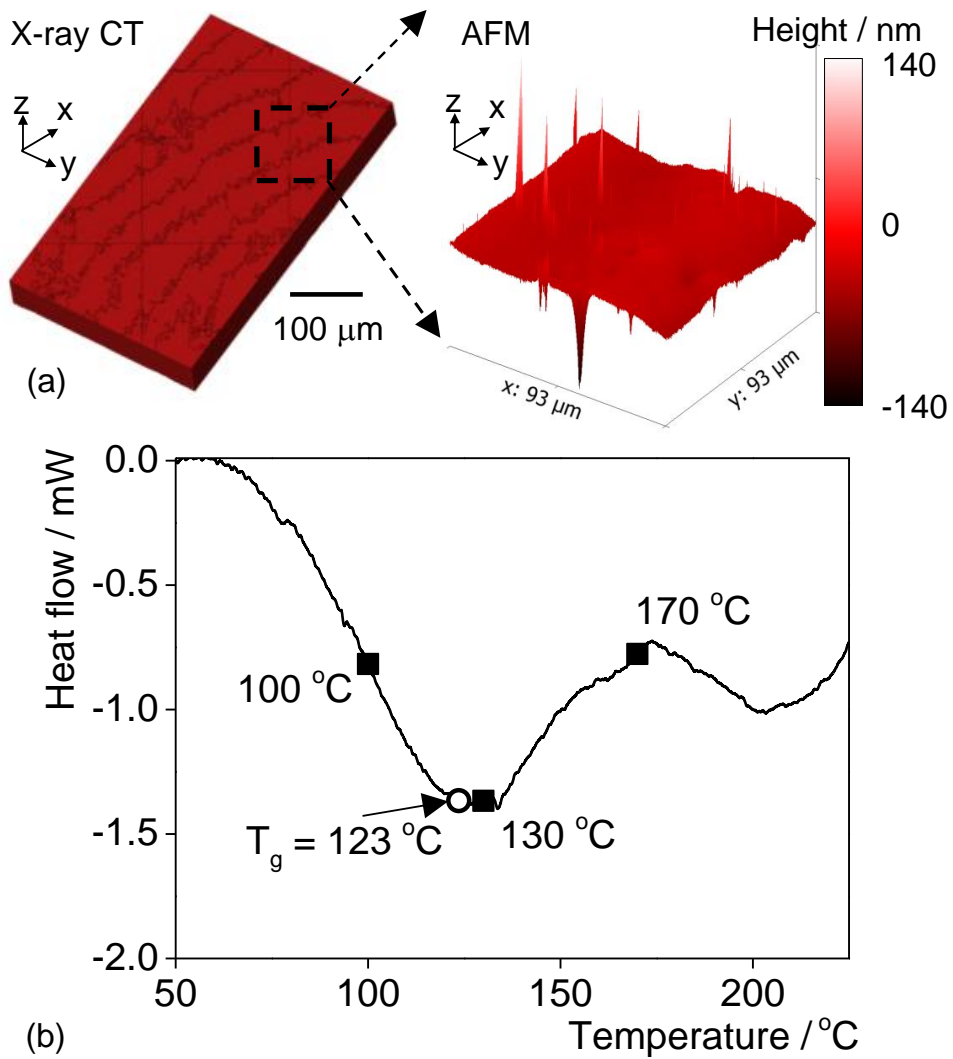


Figure 4. Characterisation of the NRE-212 Nafion membrane (a) X-ray CT and AFM of the Nafion membrane; (b) DSC of the Nafion membrane done in N₂ atmosphere, with instrument baseline correction.

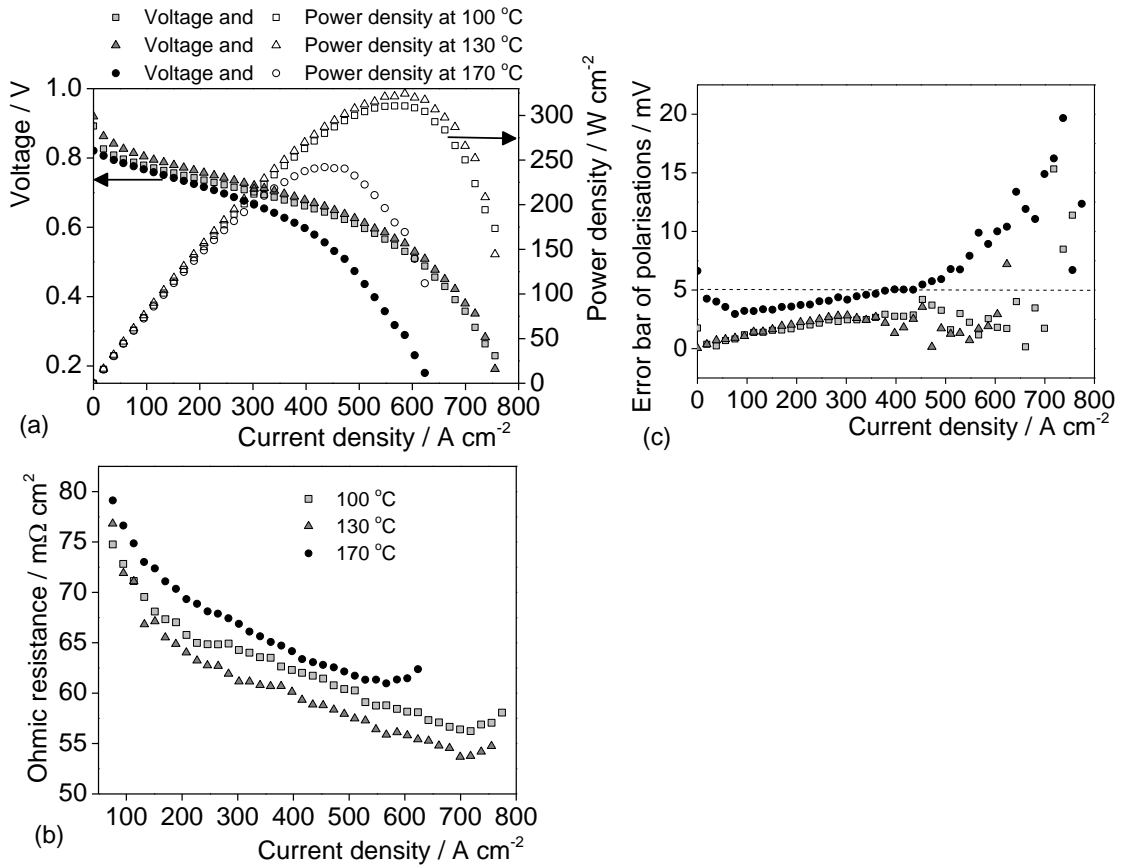


Figure 5. Effect of hot pressing at 100 °C, 130 °C and 170 °C onto the voltage and power density (a) and the Ohmic resistance (b); (c) error bar between the two repeats of the polarisation at 100 °C, 130 °C and 170 °C.

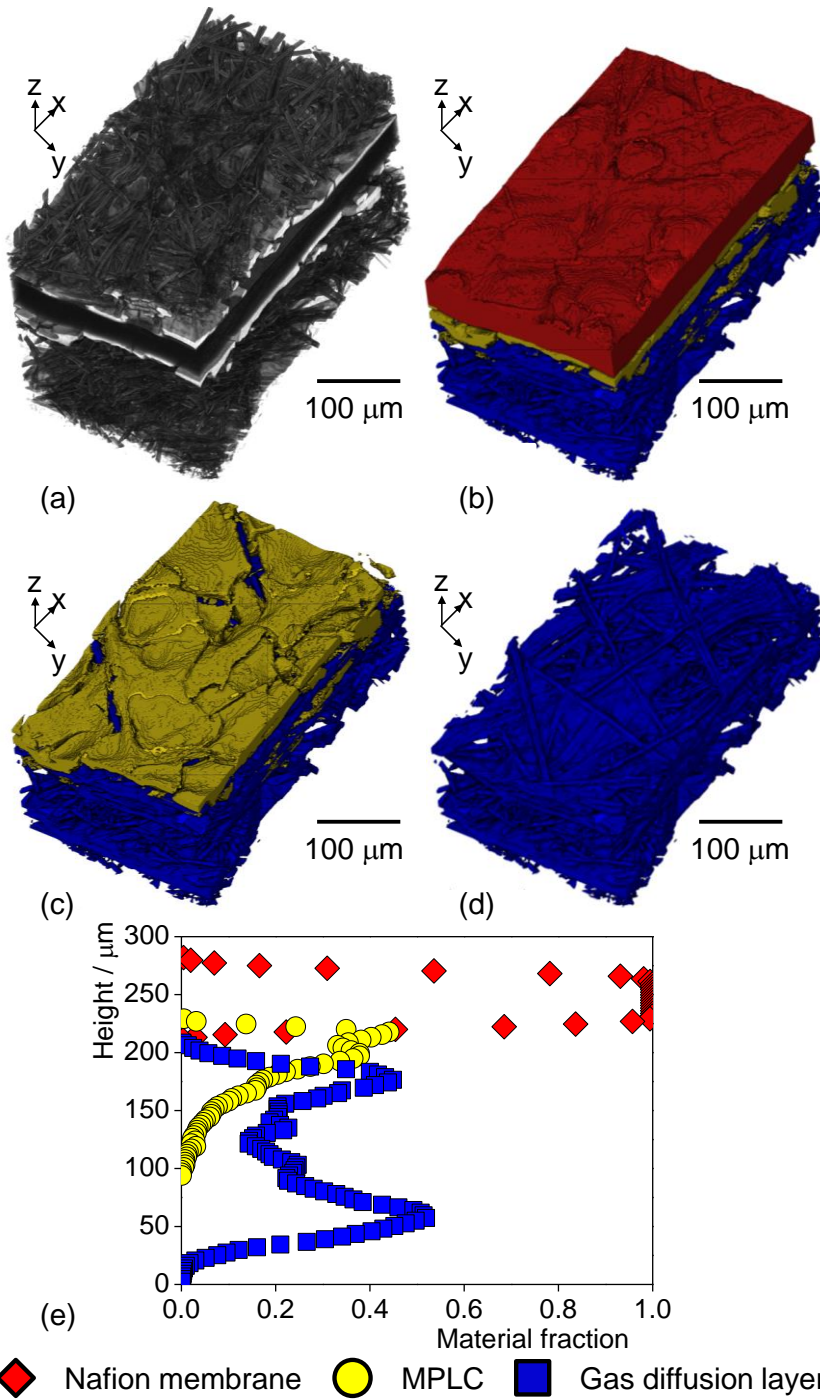


Figure 6. X-ray CT of the hot pressed membrane onto the GDE at 100 °C. (a) Volume rendering of the entire structure; (b-d) segmented Nafion (red), MPLC (yellow) and GDL (blue) (pixel size: 760 μm, field-of-view: 300 μm × 500 μm); (e) solid fraction of the three materials.

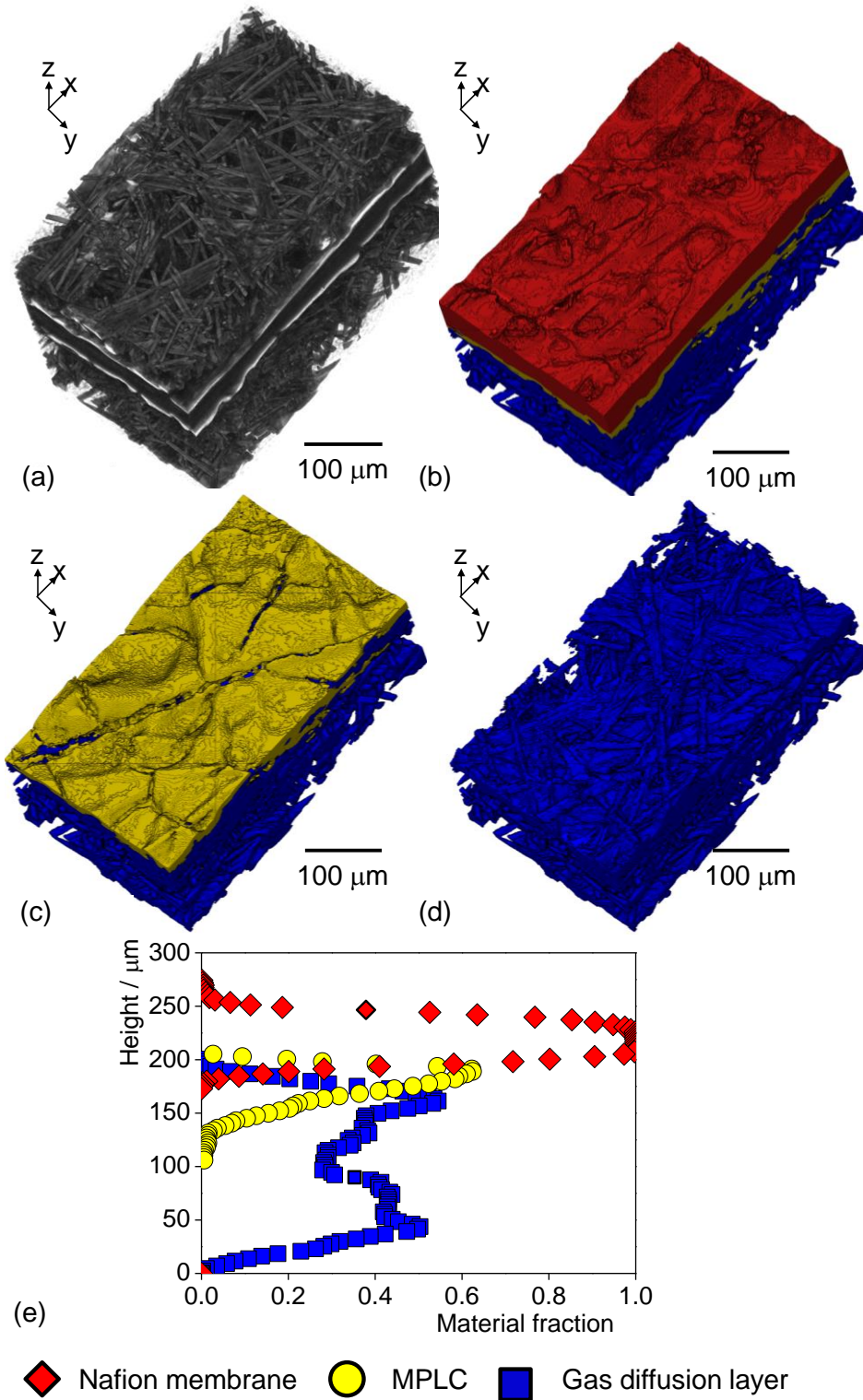


Figure 7. X-ray CT of the hot pressed membrane onto the GDE at 130 °C. (a) Volume rendering of the entire structure; segmented Nafion (red), MPLC (yellow) and GDL (blue) (pixel size: 760 μm, field-of-view: 300 μm × 500 μm); (e) solid fraction of the three materials.

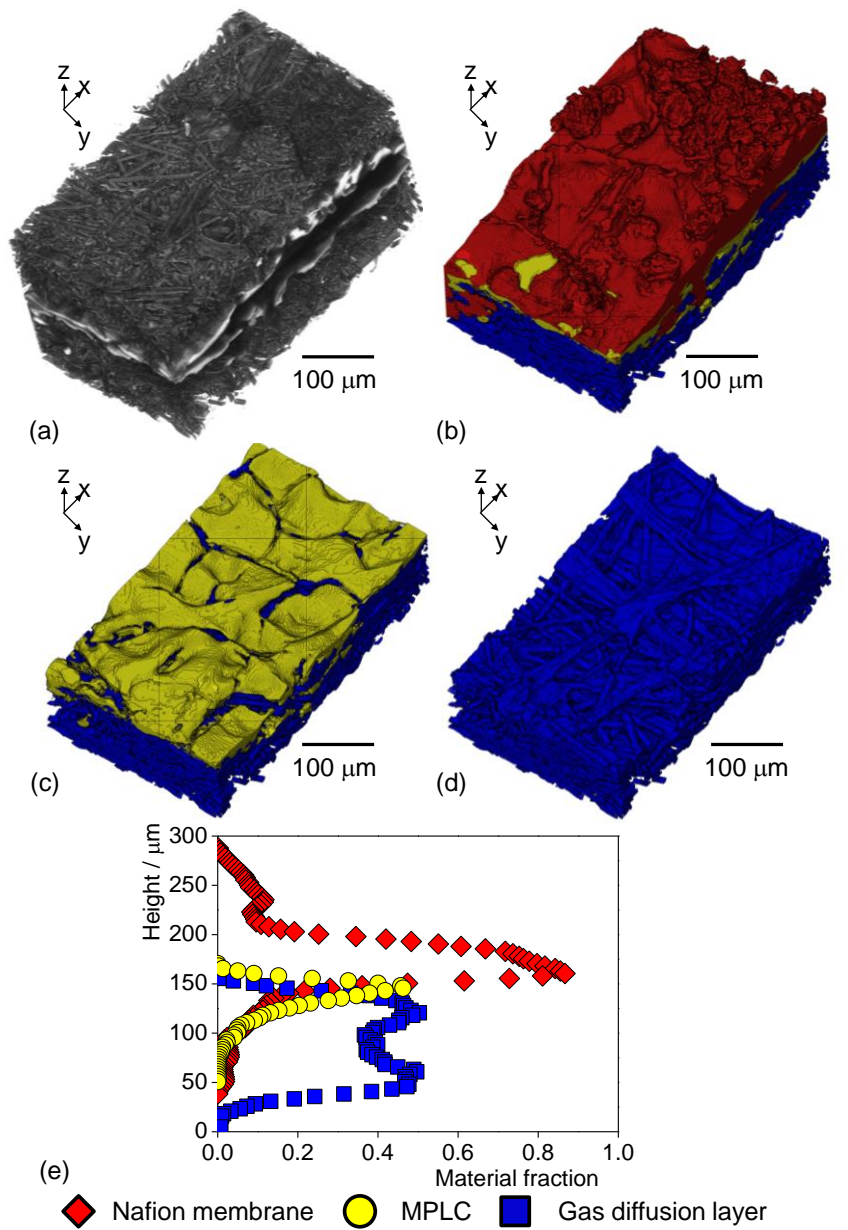


Figure 8. X-ray CT of the hot pressed membrane onto the GDE at 170 °C. (a) Volume rendering of the entire structure; (b-d) segmented Nafion (red), MPLC (yellow) and GDL (blue) (pixel size: 760 μm, field-of-view: 300 μm × 500 μm); (e) solid fraction of the three materials.

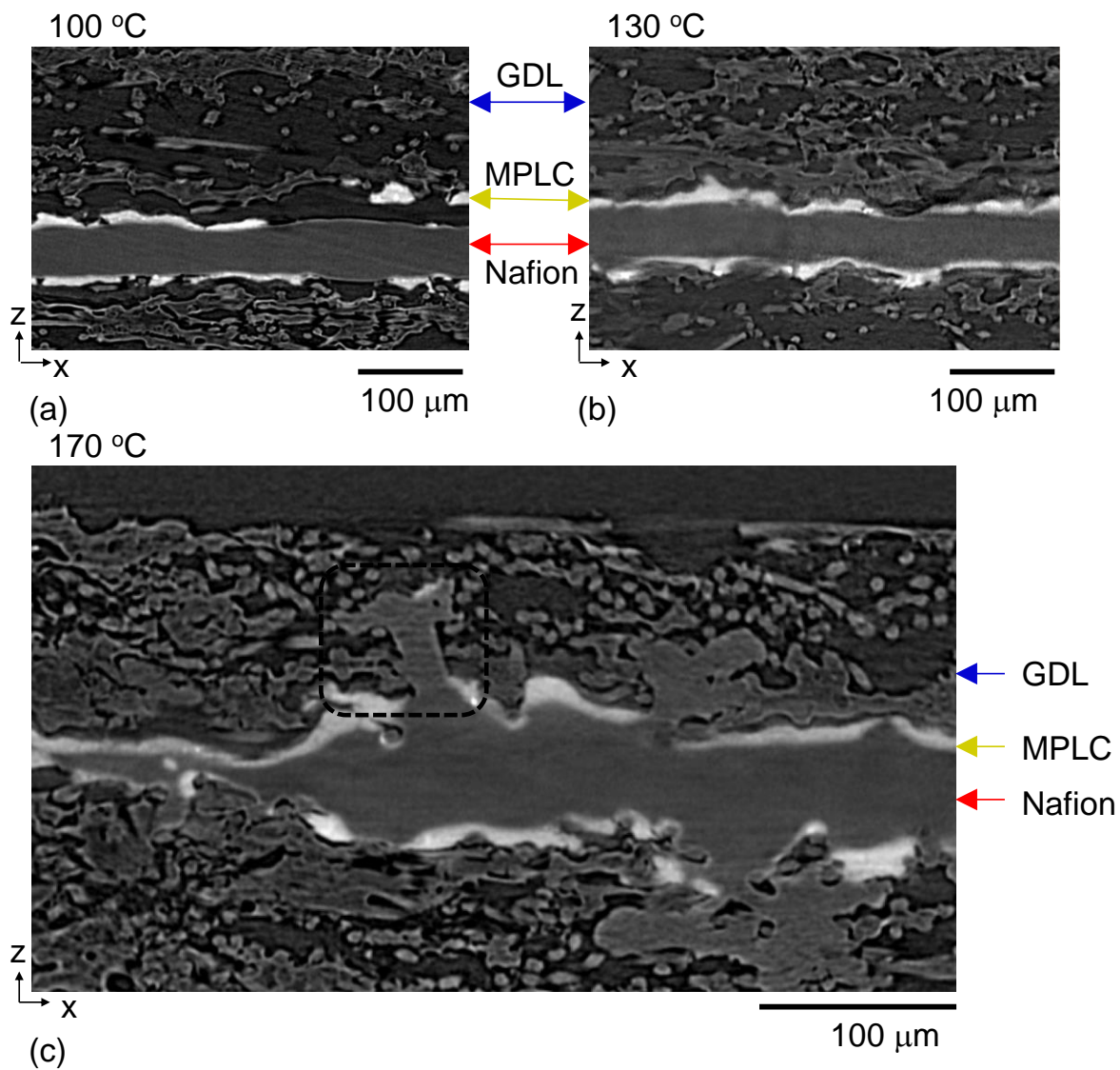


Figure 9. X-ray orthoslices at 100 °C, 130 °C and 170 °C. The dashed rectangle serves as guidance for the eye for an area where the Nafion has penetrated the MPLC and GDL at 170 °C, and contains a portion of the catalyst layer (white) deep into the GDL structure.

Table 1. Summary of parameters describing microstructural change before and after hot pressing at 100 °C, 130 °C and 170 °C.

		Properties before hot pressing	After Hot pressing 100 °C	After hot pressing 130 °C	After hot pressing 170 °C
Nafion 212 thickness t_{Nafion} (μm)		50.8	44 \pm 3	43 \pm 6	29 \pm 19
Nafion 212 roughness factor r_{Nafion} ($\mu\text{m}^2/\mu\text{m}^2$)		1.02 \pm 0.02 (AFM)	1.15 (X-ray CT)	1.33 (X-ray CT)	2.98 (X-ray CT)
MPLC outer surface roughness factor ($\mu\text{m}^2/\mu\text{m}^2$)		1.54	1.26	1.32	1.48
Normalised contact area ($\mu\text{m}^2/\mu\text{m}^2$)	$A_{GDL/MPC}$	0.35	0.39	0.83	0.76
	$A_{GDL/Nafion}$	0	0	2.1×10^{-3}	0.40
	$A_{MPLC/Nafion}$	0.59	0.59	1.28	1.45
Width of the surface cracks in the MPLC (μm)		14 \pm 4	12 \pm 3	7 \pm 3	13 \pm 7